Lithium Adsorption on Graphene at Finite Temperature

note finali coverpage

(Article begins on next page)

20 May 2024

Lithium Adsorption on Graphene at Finite Temperature

Yusuf Shaidu,[†,‡] Emine Kucukbenli,[‡] and Stefano de Gironcoli[*,‡]

†*The Abdus Salam International Centre for Theoretical Physics, Strada Costiera 11, 34151*
Trieste Italy

‡*International School for Advanced Studies, Via Bonomea 265, 34136 Trieste, Italy*

E-mail: degironc@sissa.it

Abstract

The increasing demand for high energy density lithium ion batteries motivates a search for alternative electrode materials. Experimentally obtained graphene-based structures have been suggested to replace the state-of-the-art graphitic anode. For a thorough characterization of Li adsorption on graphene, we study the interaction of Li with graphene both at zero and finite temperatures. The zero temperature study was carried out by means of density functional theory (DFT) accounting for van der Waals (vdW) interactions while the finite temperature behavior was studied by Monte Carlo techniques with a DFT-derived Li-graphene interaction potential constructed via cluster expansion method. Our calculations reveal two distinct types of orderings of Li on graphene, Li-gas (dispersed Li-ion) and Li-cluster phases. The zero temperature calculations show that, even when vdW is included, the Li-graphene interaction is mainly electrostatic and phase separation to pristine graphene and bulk Li is energetically most favorable. At non-zero temperatures though, entropy contribution to free energy allows the lesser-ordered Li-gas and Li-cluster states to be more favorable at sufficiently low concentrations: At temperatures below $400\,\mathrm{K}$ and concentrations below 1Li:6C Li-gas and Li-cluster phases co-exist, while at higher concentrations only clusters remain stable. At temperatures above $400\,\mathrm{K}$ Li-gas phase can be stabilized with respect to Li-cluster or Li bulk at higher concentrations. Furthermore, small variations in chemical potential are shown to be enough to change that concentration threshold. Finally we show that the Li-cluster phases can have Li-island or Li-stripes ordering; however Li-stripes appear due to the finite size of the simulation cell and therefore, the Li-island phase is expected to dominate in the thermodynamic limit instead.

1. INTRODUCTION

The need for high energy-density Lithium ion battery (LIB) technology is increasing with the increasing demand for portable electronic devices and electric vehicles. While alternatives are being developed, graphite has long been the typical negative electrode used in LIBs.[1–3] During charging, the Li^+ ions intercalate between the layers of graphite in a ratio of 1Li:6C,[4] corresponding to a theoretical specific capacity of 372 mAh/g. Graphene, the single layer of carbon atoms in graphite,[5] is also suggested as potential Li host by itself[6] due to doubling of the surface accessible for Li adsorption. However, Pollak *et al.*[7] presented experimental evidence that Li capacity of a single-layer graphene is less than that of graphite due to strong Coulomb repulsion between Li ions on either side of the graphene layer. Nevertheless, experimental studies on non-graphitic arrangements of graphene have reported high Li-capacity in the 540-1500 mAh/g range,[6,8–12] surpassing the graphite anode. These experimental observations suggest an apparent discrepancy where the building block, graphene, fails to host significant amount of Li ions while graphene-based materials can be very promising anode materials, despite a major amount of single-layer graphene presence within them.

Several theoretical studies based on Density Functional Theory (DFT)[13–21] attempted to elucidate the nature of high Li adsorption on graphene-based systems: Lee and Persson[13] showed that Li cannot reside on the surface of a defect-free single layer graphene in equilibrium with bulk Li metal and Li capacity would be lower than that of graphite. Li adsorption on graphene with defects, vacancies[14,15] and edges[16–18] have also been investigated and the results revealed that the binding energy of Li decreases rapidly as its position moves away from the vicinity of the edges and defects, meaning that defects alone would provide a relatively small, local enhancement to adsorption. Hydrogen passivation of defects results in positive binding energy[15] with respect to bulk Li, similar to that of defect-free graphene, making the capacity of H-passivated defective graphene inferior to that of graphite. Therefore these theoretical studies do not provide a satisfactory explanation for the experimental observation of high Li uptake of graphene-based systems. It is important to note that these

works explore single, dilute Li ion adsorption configurations. Studies on compact Li clusters show instead that the energetic stability of Li clusters on graphene increases with the cluster size[19–21] suggesting that the formation of compact Li clusters could explain the reported high Li uptake by graphene materials. However, the possibility of high Li uptake due to formation of Li clusters is not necessarily desired since a continuous growth of clusters on the anode may result in reduced battery efficiency and compromise safety of the battery. Therefore the desired mechanism for high Li uptake is a dispersed configuration rather than clustering, especially if cluster growth is thermodynamically favored. Noting that the theoretical calculations mentioned so far were done at zero temperature while LIBs operate at room temperature or above, it is important to investigate whether thermal effects may favor dispersed Li configurations or may stabilize small cluster sizes.

Thermal effects on the adsorption of Li clusters on graphene were previously estimated in Refs. 20 and 21 by choosing a random configuration as a reference, approximating the entropy through it, and by neglecting the configurational entropy of the clusters. In these studies, the formation of Li clusters was found to be stable against random distribution of Li ions for high concentration (1Li:6C) at 300 and 500 K; while at low concentrations (1Li:72C and lower) a disperse configuration was favored. Furthermore, Liu *et al.*[20] estimated nucleation barriers as high as approximately 15 eV for a cluster to form in dilute configurations (1Li:162C), suggesting that thermal effects may indeed stabilize disperse configurations. However these findings rest on a heavily approximated description of entropy, which is particularly critical in understanding the thermal effects.

In this work we systematically study Li adsorption on graphene in a wide range of concentrations and temperatures, using Monte Carlo simulations to accurately describe the configurational entropy. The paper is organized as follows: in Section 2 A, the computational details used for the zero temperature studies are presented, while the methods employed for finite temperature studies, the cluster expansion methods, the Monte Carlo techniques and thermodynamic integration, are presented in Section 2 B, C and D respectively. The

results of the zero temperature studies are presented and discussed in Section 3 A. The finite temperature results are discussed in Section 3 B, C and D. Finally, we present our conclusions.

2. COMPUTATIONAL METHODS

2A. Zero temperature properties

We examined Li adsorption on graphene at zero temperature by means of Density Functional Theory (DFT)[22,23] within the planewave-Projector Augmented Wave (PAW) [24] framework using the Quantum ESPRESSO package.[25,26] The PAW pseudopotentials were generated from the pslibrary.1.0.0.[27] Kinetic-energy cutoffs of 125 Ry and 500 Ry were used in the expansion of wavefunctions and charge density respectively. With these parameters, a total energy convergence of 0.1 mRy/atom was achieved. The revised Vydrov and van Voorhis (rVV10)[28,29] exchange-correlation functional was used to account for non-local van der Waals interactions. For comparison, we also performed calculations using generalized gradient approximation in the Perdew-Burke-Ernzerhof (PBE) parametrization.[30] The total energy calculations of Li-graphene were done in graphene supercells with dimensions ranging from 2x2 to 8x8 primitive cells. Brillouin zone was sampled uniformly according to the Monkhorst-Pack[31] procedure with Methfessel-Paxton[32] smearing of 0.02 Ry. A 30x30x1 mesh centered around gamma point was found to be sufficient for 0.1 mRy per atom convergence of total energy of graphene primitive unit cell. Calculations with different supercells were done conserving this sampling density.

The in-plane lattice parameters of pristine graphene were fully optimized while the spacing between periodic replicas along the perpendicular direction was fixed at 20 Å, at which the effect of periodic replicas are shown to be negligible (see Supporting Information Available). In each configuration, all internal coordinates were relaxed until force components were reduced below 0.1 mRy/Bohr. The optimized lattice parameter of graphene with

rVV10 functional is $2.470\,\text{Å}$ ($2.466\,\text{Å}$ with PBE), in good agreement with previous DFT calculations of $2.463\,\text{Å}$,[15] $2.45\,\text{Å}$,[16] $2.47\,\text{Å}$,[33] $2.46\,\text{Å}$,[34] as well as the experimental in-plane lattice parameter of graphite $2.459\,\text{Å}$.[35]

The stability of Li upon adsorption on graphene was investigated by measuring the adsorption energy per Li ion, E_{ad}, with respect to bulk Li:

$$E_{ad}(n) = \frac{E(n) - E(n = 0) - nE_{Li}}{n} \tag{1}$$

where $E(n)$ is the calculated total energy of the Lithium-adsorbed graphene of a given supercell size, $E(n = 0)$ is the pristine graphene of same supercell size and E_{Li} is the energy per atom in bulk Li in the body centred cubic (bcc) phase. When indicated as such, we also report adsorption energy with respect to the isolated Li atom in vacuum for comparison with literature. The energy difference between Li in vacuum and bulk is the cohesive energy which is calculated as $1.586\,\text{eV}$ for rVV10 and $1.561\,\text{eV}$ for PBE.

2B. Cluster expansion methods

In order to carry out an exhaustive sampling of the phase space at finite temperature, we construct a computationally affordable description for the configurational energy using cluster expansion (CE) method: We map the Li adsorption on graphene into a lattice model and describe the energy of a given configuration of Li-graphene system as a generalized Ising-like interaction energy. To simplify the model, we restrict Li adsorption geometry to 2D and the adsorption site to the hollow site (the hexagon centers), H of graphene. Occupation of other sites (the top of a carbon, T and the bridge, B, sites) and 3D Li configurations are beyond the scope of this work. Such a 2D model is compatible with experimental observations in which limited spacing between graphene sheets is found to prevent compact 3D Li growth.[6,8,36]

In this model, a Li occupation number c_i is assigned to each site i ($c_i = 0$ if site i is empty

and $c_i = 1$ if site i is occupied by a Li atom, equivalent to the more common convention where spin-like variables $\sigma_i = \pm 1$ are used) and a configuration is defined as $C_N = \{c_i\}$, with $i = 1, ..., N$ for N lattice sites. The configurational energy E_{CE} is then written as a linear combination of correlation functions $\Pi_f(C_N)$ with each function describing a figure f (a cluster of lattice points), the corresponding coefficient in the linear expansion J_f being called the effective cluster interaction (ECI):[37]

$$E_{CE}(C_N) = \sum_f J_f \Pi_f(C_N) = \sum_f J_f \prod_{i \in f} c_i. \tag{2}$$

In a lattice with N sites, there are 2^N figures: N 1-body figures, $\binom{N}{2}$ 2-body figures, $\binom{N}{3}$ 3-body figures etc. Therefore, the expansion in Eq. 2 has 2^N ECI's, one for each figure, requiring in principle 2^N total energy calculations to determine all the ECI's and construct an accurate CE model. Exploiting crystal symmetries (translational and rotational) and physical arguments of locality of the interaction (short-distance compact figures are expected to be more important than more-distant or dispersed ones) the number of figures to be included in the energy expansion can be constrained, leading to a limited number of independent parameters, thus requiring only a small number of total energy calculations as reference.

In this work, we include the compact figures up to 4-body (see Fig. 1): on-site term (figure 1), 2-body first, second and third nearest-neighbor terms up to a $2a_0$ distance, where a_0 is the lattice constant of graphene, (figures 2a,2b and 2c), a 3-body and a 4-body term (figures 3 and 4, respectively). In addition to these, for two body interactions beyond $2a_0$, we include an effective electrostatic dipole-dipole term in the energy description. This term is set to decay with the third power of Li-Li distance, truncated for simplicity at $20a_0$. The final expansion for the total configuration energy is written as follows:
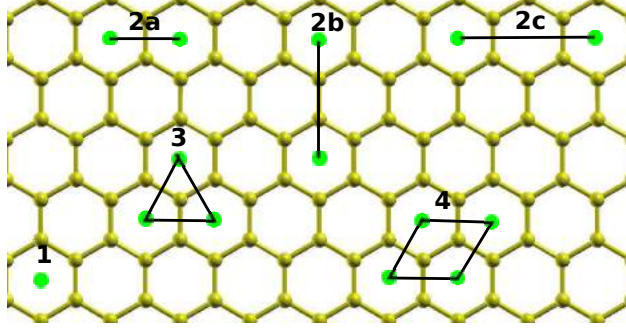
Figure 1: Figures included in the cluster expansion: (1) the on-site, (2) the 2-body figures between (2a) first nearest neighbors, (2b) second nearest neighbors, and (2c) third nearest neighbors, (3) the most compact 3-body figure, (4) the most compact 4-body figure.

$$
\begin{aligned}
E_{CE}(C) \;=\; & J_1 \sum_{i \in f_1} c_i + \frac{1}{2} \sum_{p=a,b,c} J_{2p} \sum_{\{ij\} \in f_{2p}} c_i c_j \\
+ \; & \frac{J_3}{6} \sum_{\{ijk\} \in f_3} c_i c_j c_k + \frac{J_4}{24} \sum_{\{ijkl\} \in f_4} c_i c_j c_k c_l \\
+ \; & \frac{J_{dd}}{2} \sum_{ij,|\mathbf{r}_i-\mathbf{r}_j|>2a_0} \frac{\alpha_i \alpha_j}{|\mathbf{r}_i - \mathbf{r}_j|^3} c_i c_j
\end{aligned}
\tag{3}
$$

We use two parameters, J_{dd} and α, to model the effective electrostatic interaction figures. While J_{dd} is the same for all sites, α parameter is used to distinguish the electrostatic interaction strength in the case of the isolated atom and the clusters:

$$
\alpha_i =
\begin{cases}
1 & \text{if } NN_i = 0 \\[2mm]
\gamma & \text{if } NN_i > 0
\end{cases}
\tag{4}
$$

where γ is an adimensional scalar parameter and NN_i is the number of occupied nearest neighbors to site i. This electrostatic description of the model is motivated by the electrostatic behavior of Li-graphene interactions analyzed in Section 3 A.

The interaction energy given by equation 3 is then fitted to DFT adsorption energies to obtain all the eight parameters of the model. A total of 25 fully relaxed configurations were used for the fitting. These configurations covered a variety of Li ion environments from single Li adatom to small cluster cases. See Supplementary material for a detailed description of

these configurations and the fitting procedure.

2C. Grand-canonical Monte Carlo

The finite temperature behaviour of Li interactions with graphene was investigated via Grand-Canonical Monte Carlo (GCMC) simulations which allow to compute the thermodynamic properties of the system at any given chemical potential, μ, and temperature, T. The GCMC results in this work were obtained with a 20x20 simulation cell of graphene containing 800 carbon atoms and 400 H-sites, while finite size effects were explored on a 25x25 cell.

The configuration space is sampled as follows: *i)* an adsorption site is selected at random; *ii)* an attempt to reverse its state is performed, i.e. adding a Li to the site if empty or removing it if occupied; *iii)* the proposed move is accepted according to Metropolis[38,39] rule with probability $\min[1, \exp(-\beta(\Delta E - \mu \Delta N))]$, with $\beta = 1/(k_B T)$, $\Delta E = E_{new} - E_{old}$, $\Delta N = N_{new} - N_{old}$, and E_{new}, E_{old}, N_{new}, N_{old} are the configurational energies and number of adsorbed Li atoms of the new and the old configurations, respectively. Each attempt to add (delete) a Li to (from) a randomly selected site is considered a Monte Carlo step.

The temperature-chemical potential plane was explored with a series of unidimensional scans. Chemical potential scans were done between -0.2 and $0.2\,\text{eV}$ at intervals of $10\,\text{meV}$ while temperature scans were carried out between 400 and $4000\,\text{K}$ at intervals of $50\,\text{K}$. In each scan, simulations were performed in sequence so that each simulation started from the final configuration of the preceding one. Thus, 1.5 million Monte Carlo equilibration steps were enough to equilibrate the system at each chemical potential/temperature pair. Statistics were then accumulated over 2 millions steps and used for the evaluation of the averages. When the the simulation approached a phase transition, Li concentration, $x = \langle \sum_i c_i \rangle / N$, is observed to display sudden jumps and caused large uncertainties in the statistical averages calculated.

A few exploratory chemical potential scans at intermediate temperatures allowed us to

identify the relevant phase transitions of the system and the corresponding chemical potential ranges by monitoring discontinuities in Li concentration. Then we performed a careful chemical potential scan at very high temperature (4000 K) where all the phases are connected and no concentration discontinuity is observed. Subsequently, we perform temperature (annealing) scans at a number of fixed chemical potentials, which give us access to initial configurations for further chemical-potential scans for the different phases at various temperatures. In this way each (μ, T) state of a phase can be connected to any other (μ', T') state of another phase through a path in $\mu - T$ plane without discontinuous jumps of the relevant conjugate thermodynamical quantities, i.e. concentration and internal configurational energy. This allows us to compute the free energy of each phase on a common energy scale and compare their relative stability through thermodynamic integration.

2D. Thermodynamic integration

The total differential of the grand potential per site, $\Phi(\mu, \beta)$ can be used to obtain the following relation:

$$d(\beta\Phi) = \left(\frac{\langle E \rangle}{N} - \mu x\right) d\beta - \beta \, x \, d\mu. \tag{5}$$

where β is the inverse temperature $1/k_B T$.

At constant temperature, the integration of Eq. 5 from a reference chemical potential μ_0 to a desired chemical potential μ, gives the grand potential per site $\Phi(\mu, \beta)$ relative to the reference value, $\Phi(\mu_0, \beta)$, as:

$$\Phi(\mu, \beta) = \Phi(\mu_0, \beta) - \int_{\mu_0}^{\mu} x \, d\mu. \tag{6}$$

This expression is valid provided the chemical potential interval (μ_0, μ) spans a single phase and the resulting $\mu \rightarrow x$ mapping is invertible. The Helmholtz free energy per site of the phase under examination can then be obtained from the Legendre transform
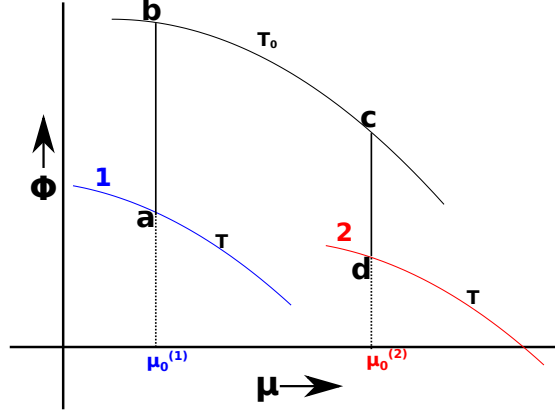
Figure 2: Thermodynamic integration: The free energy difference between phase 1 in a $(\mu_0^{(1)}, T)$ and phase 2 in d $(\mu_0^{(2)}, T)$ can be obtained using integration along the a $\to$ b $\to$ c $\to$ d path.

$$F(x, \beta) = \min_{\mu} \left\{ \Phi(\mu, \beta) + \mu x \right\} = \Phi(\mu(x), \beta) + \mu(x)x. \tag{7}$$

In order to compare the Helmholtz free energy of two phases at a given temperature, the difference between the reference grand potential values of the two phases, $\Phi(\mu_0^{(1,2)}, \beta)$, must be determined. This can be achieved by thermodynamic integration on the path schematically illustrated in Fig. 2 that connects phase space point a to d. Point a corresponds to the reference point $(\mu_0^{(1)}, \beta)$ of phase 1, and point d corresponds to the reference point $(\mu_0^{(2)}, \beta)$ of phase 2. Integration of equation 5 over a smooth path without discontinuity is ensured by moving along the path a $\to$ b $\to$ c $\to$ d:

$$
\begin{aligned}
\beta \Delta \Phi^{(1,2)}(\beta) &= \int_{\beta}^{\beta_0} \left(\frac{\langle E^{(1)} \rangle}{N} - \mu_0^{(1)} x \right) d\beta \\
&\quad - \beta_0 \int_{\mu_0^{(1)}}^{\mu_0^{(2)}} x \, d\mu \\
&\quad + \int_{\beta_0}^{\beta} \left(\frac{\langle E^{(2)} \rangle}{N} - \mu_0^{(2)} x \right) d\beta,
\end{aligned}
\tag{8}
$$

where $\Delta \Phi^{(1,2)}(\beta) = \Phi(\mu_0^{(2)}, \beta) - \Phi(\mu_0^{(1)}, \beta)$ is the free energy difference at inverse temperature β between phase 1 at chemical potentials $\mu_0^{(1)}$ and phase 2 at chemical potentials $\mu_0^{(2)}$ and the

11

auxiliary inverse temperature $\beta_0 = 1/(k_B T_0)$ is such that both the average energy, $\langle E \rangle$, and and the Li concentration, x, vary continuously along the path connecting the two phases. We found $T_0 = 4000\,\mathrm{K}$ to be sufficient for this purpose.

3. RESULTS AND DISCUSSION

3A. Li adsorption at zero temperature

We start by analyzing the energetic stability of the three main binding sites of graphene, namely the top (T), the bridge (B) and the hollow (H) sites (see Fig. 3). The results in
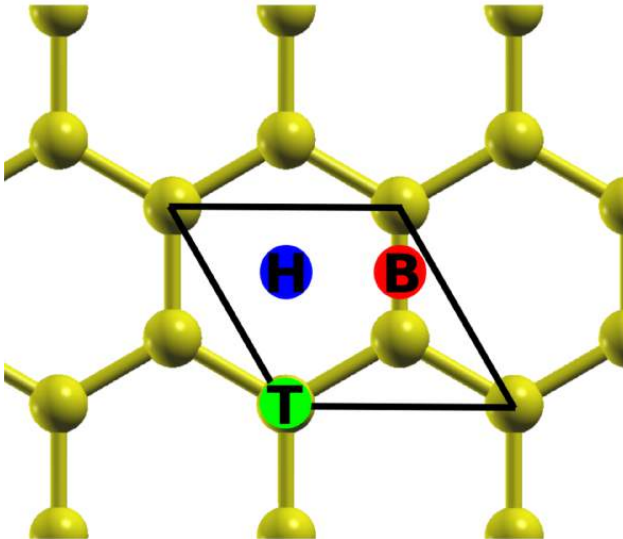

Figure 3: Lithium binding sites on graphene are commonly named as hollow (H), top (T) and bridge (B) sites. The black lines indicate the primitive unit cell of graphene.

Table 1 shows that Li atom binds preferably to the H site, in agreement with previous DFT calculations.[14,16,33,40] The energy difference, ΔE_{ad} between H site and that of B and T is beyond a few multiples of $k_B T$ at room temperature, and gets significantly higher at lower concentrations. Therefore at concentrations corresponding to 1Li:8C (single Li atom in a 2x2 supercell) and lower, Li atoms would be expected to occupy mainly the H site. We limit our investigations to Li adsorption on the H site in the rest of the discussion.

We then investigate the energetic stability of small Li-clusters as a function of supercell

Table 1: The adsorption energy of Li at the hollow site of graphene, E_{ad}, calculated with respect to bulk Li in bcc phase (values referenced to isolated Li atom are given in parenthesis). ΔE_{ad} is the adsorption energy difference for bridge and top sites with respect to the hollow site. All energy values are in eV.

cell size	E_{ad}	$\Delta E_{ad}(B)$	$\Delta E_{ad}(T)$
PBE			
2x2	0.712 (-0.849)	0.159	0.167
3x3	0.646 (-0.915)	0.310	0.327
4x4	0.468 (-1.093)	0.317	0.339
6x6	0.301 (-1.260)	0.294	0.316
7x7	0.270 (-1.291)	0.286	0.310
9x9	0.227 (-1.334)	0.283	0.305
rVV10			
2x2	0.625 (-0.961)	0.134	0.142
3x3	0.652 (-0.934)	0.241	0.256
4x4	0.485 (-1.101)	0.294	0.314
6x6	0.328 (-1.258)	0.267	0.288
7x7	0.290 (-1.296)	0.268	0.289
9x9	0.253 (-1.333)	0.257	0.280
Literature			
PBE[40]			
2x2	- (-0.925)	-	0.177
3x3	- (-1.025)	-	0.341
PBE[33]			
4x4	- (-1.096)	0.322	0.342
PBE[14]			
6x6	0.315 (-1.290)	0.285	0.308
7x7	0.298 (-1.308)	0.301	0.320
9x9	0.190 (-1.416)	0.356	0.376
LSDA[41]			
4x4	- (-1.567)	0.327	0.376

size (see Fig. 4). For all the concentrations considered, the adsorption energy calculated with respect to bulk Li is positive, which suggests that Li may not reside on the surface of a defect-free single layer graphene in equilibrium with Li-metal, which is in agreement with previous DFT calculations.[13] The stability of bulk Li can explain why the adsorption energy per atom decreases as the clusters get larger for a fixed cell size, while a qualitative difference between single adatom and cluster behavior can be observed.

For single Li adatom case, the general trend of the adsorption energy at different binding sites is the same for rVV10 and PBE functionals (see Table 1). Similarly, both functionals capture the correlation with cell size qualitatively the same way. The most significant differ-
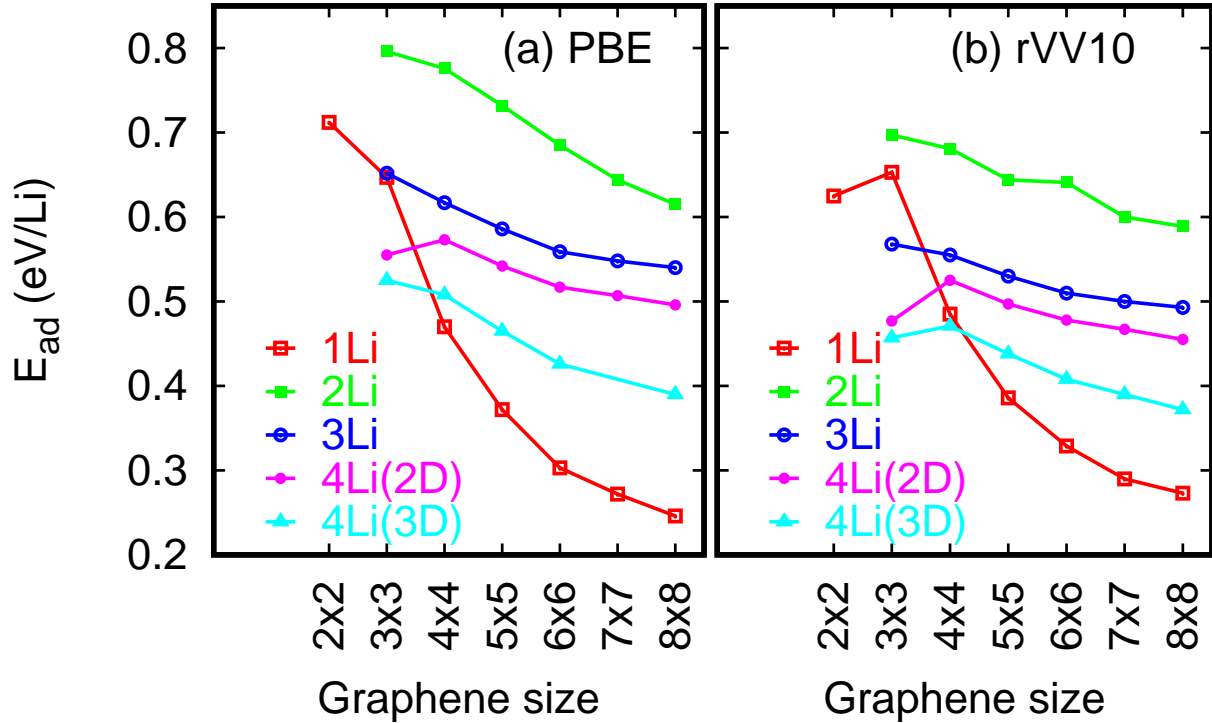
Figure 4: Adsorption energy of Li on graphene as a function of graphene cell size with (a) PBE and (b) rVV10 functionals, referenced to bulk Li in the bcc phase. 1Li is the Li adatom on the corresponding supercell. 2Li, 3Li, 4Li(2D) and 4Li(3D) represent Li clusters, namely Li-dimer, Li-trimer, planar Li-tetramer and pyramidal Li-tetramer respectively.

ence between functionals is observed in the Li cluster configurations where rVV10 functional results in significantly lower (less positive) binding energies. Comparing our results with the single adatom binding energy analysis of var der Waals (vdW) functionals in Ref. 42, where a variation of about $100\,\mathrm{meV/Li}$ was observed depending on the vdW treatment, it can be argued that details of how vdW interaction is treated are important for Li-graphene systems at all length scales. This is likely a combined effect of the use of different vdW schemes *and* the practice of adjusting the overall exchange and correlation description when using vdW-aware functionals.

When fixed concentration is considered, the lower binding energy with rVV10 favors the formation of Li clusters over homogeneous distribution of Li adatoms. For instance, the adsorption energy of Li adatom in a 2x2, 3x3, 4x4 supercells are higher than that of Li-

clusters with four atoms in 4x4, 6x6, 8x8 supercells respectively. Same tendency is observed with PBE, although less consistently. In the rest of the discussion, we refer to the results obtained with rVV10 functional.
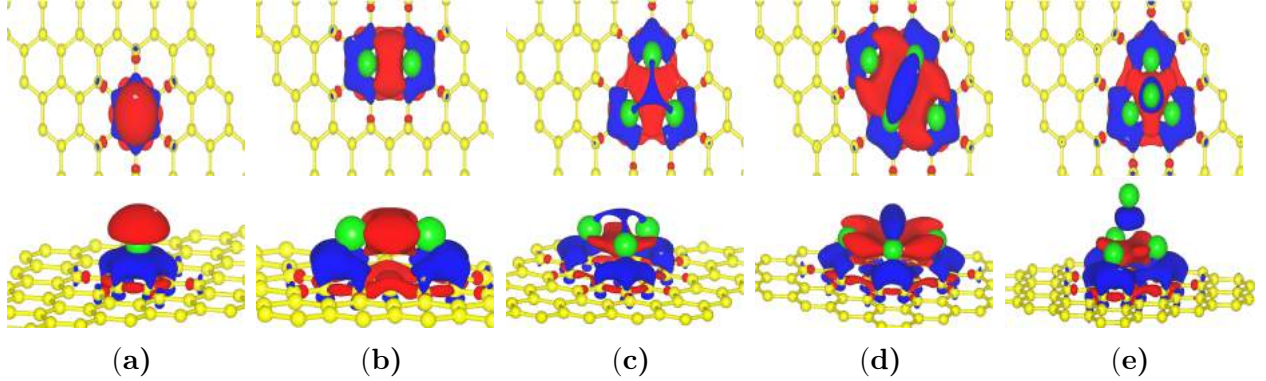

Figure 5: Charge density difference with rVV10 functional upon adsorption of (a) Li adatom (b) Li-dimer (c) Li-trimer (d) Li-tetramer (planar) and (e) Li-tetramer (pyramidal) on a 6x6 graphene supercell. Yellow and green spheres represent carbon and lithium atoms respectively. Red and blue regions indicate respectively the electronic charge depletion and accumulation. The surfaces are plotted at an isovalue of 0.002 $e/(a.u)^3$.

The observation of decreasing adsorption energy with increasing cell size in Fig. 4 implies the presence of electrostatic repulsion between adsorbates in adjacent simulation cells. This repulsive interaction is more evident for the single Li adatom case indicating that the dipole per atom due to charge transfer in Li-graphene system is more pronounced for this configuration.

In order to gain further insight, we compute the charge density difference due to lithium adsorption:

$$\Delta\rho = \rho(graphene + nLi) - \rho(graphene) - \rho(nLi) \tag{9}$$

where $\rho(graphene + nLi)$, $\rho(graphene)$ and $\rho(nLi)$ are the charge density of Li-graphene composite, graphene supercell of equal size as the composite and Li-cluster in the same optimized position as in the composite system respectively, and n is the cluster size. The results for different Li configurations on a 6x6 graphene supercell in Fig. 5 show significant charge transfer between the Li atoms and graphene. In the case of Li adatom, the electrons

transferred to graphene are localized on the hexagon upon which the Li atom is adsorbed, creating a net dipole (Fig. 5a). In the case of Li clusters (see Fig. 5b-e), the charge distribution is significantly different from that of Li-adatom since the positive charge is delocalized over the whole cluster, and not as elevated above the Li level as in the case of Li adatom. We quantify this difference by analyzing the planar average of the charge density difference per Li, $\Delta\rho_p(z)$, as a function of the perpendicular direction as shown in figure 6. A notably higher $\Delta\rho_p(z)$ is observed for Li adatom than Li-clusters. The dipole moment per Li is -0.802 eÅ for Li adatom and -0.247, -0.077, -0.125, -0.119 and -0.096 eÅ for 2, 3, 4, 5 and 6 Li-clusters respectively. This observation justifies a binary characterization of Li adsorption as single adatom versus cluster formation categories, which is utilized in the construction the interaction potential for Li-graphene system as described in Section 2B.

The adsorption energy reported in Fig. 4 also shows that isolated Li adatoms are more energetically stable than small Li-clusters at zero temperature and low concentration. This suggests that entropy may further enhance the stability of Li-adatoms over compact Li-clusters, offering the disperse Li configuration as a comparatively stable alternative to Li clusters in the case of batteries. To this end, it becomes imperative to understand the effects of temperature on the Li-graphene system.
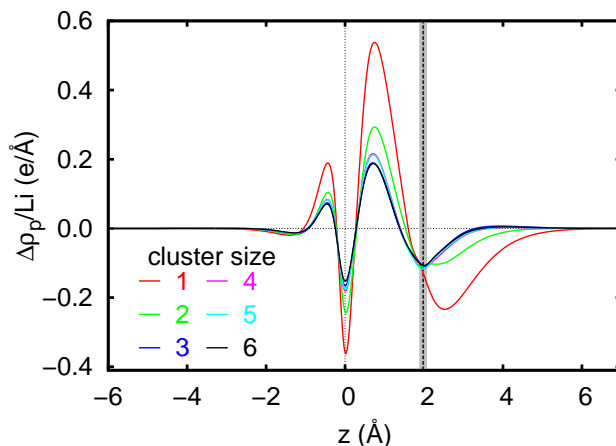

Figure 6: The planar average of the charge density difference per Li, $\Delta\rho_p(z) = \int \Delta\rho(x, y, z)dxdy$, for various 2D clusters as a function of the perpendicular distance from the graphene plane (situated at $z = 0\,\text{Å}$). The gray region shows the standard deviation of Li-heights around their average (the thick dashed line) above graphene plane.

3B. Li-graphene interaction potential

The values for parameters of the cluster expansion model are determined by fitting to the DFT adsorption energies (see Table 2). On the fitting set, a root-mean-square error of $18.0\,\mathrm{meV/Li}$ ($1.6\,\mathrm{meV/C}$) is obtained. The cross validation error calculated via leave-one-out method is found to be $30.2\,\mathrm{meV/Li}$ ($3.4\,\mathrm{meV/C}$). This error is significantly smaller than the root-mean-square deviation of $7\,\mathrm{meV/C}$ and cross validation score of $8\,\mathrm{meV/C}$ reported in Ref. 13. The on-site ECI gives approximately the adsorption energy of an isolated Li ion, as expected. Among the 2-body interactions, the nearest neighbor 2-body ECI dominates, and is positive, in line with the strong electrostatic repulsion between Li ions in nearest hexagons, also in agreement with the cluster expansion parameters of Li-graphite system reported in Ref. 43. The remaining two-body interaction terms, J_{2b} and J_{2c}, are negative, smaller in magnitude, and decrease with increasing range. This supports the assumption that, once the long range electrostatic interaction is factored out, the cluster expansion can be truncated at few nearest-neighbor distances. Compact 3- and 4-body terms are found to be significant as well for a good description of the Li-graphene interaction. We show in the supplementary material that if the 3- and 4-body terms are not included, the model accuracy is compromised and the dominant ECI becomes the on-site one in agreement with the result of Ref. 13 where these terms were not included in the expansion.

Table 2: Best fit values for the effective cluster interactions of the model in equation (3). All parameters, except γ, in eV

	J_1	J_{2a}	J_{2b}	J_{2c}	J_3	J_4	J_{dd}	γ
ECI	0.287	0.677	-0.109	-0.075	-1.429	0.234	2.086	0.383

3C. Energetics of lithium-graphene interactions

Three notable phases are observed in GCMC simulations (see Fig. 7). These phases are referred in the following as the Li-gas (G) (Fig. 7a), the Li-islands (I) (Fig.7b) and the Li-

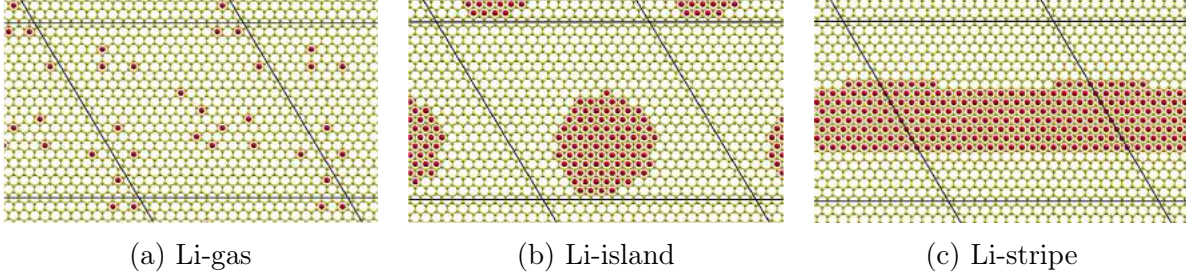(a) Li-gas   (b) Li-island   (c) Li-stripe

Figure 7: A snapshot of Li ordering on graphene of the dispersed/gas phase, the Li islands, and the Li-stripes.

stripes (S) (Fig. 7c) phases. The free energy per site of these phases at 800 K, as determined by thermodynamic integration, is shown in the upper panel of Figure 8. The minimum free energy for Li-gas phase is negative, lower than the bulk Li reference value, meaning that a small concentration of Li adatoms can stably reside on clean single layer graphene, contrary to the prediction of calculations at zero temperature. To examine the entropic origin of this stability, we compare the potential energy and entropy terms of the free energy of each phase at its minimum, i.e. at $\mu = 0$, as a function of temperature (see left panel of Figure 9).

At low temperatures, the energy term supersedes the entropic contribution in all the phases implying that free energy is positive, i.e. Li-graphene system is unstable with respect to bulk Li, in agreement with zero temperature calculations. At higher temperatures however, the entropic term dominates, stabilizing the Li-gas phase with respect to bulk Li. In the Li-islands phase, there is a cross-over from an energy-dominated region (below 1200 K) to an entropy-dominated region (above 1200 K). In the stripe phase, energy is always the dominant term in the considered temperature range, free energy is always positive, therefore this phase is less stable with respect to bulk Li. We report in the right panel of Figure 9 that by allowing a modest 10 meV shift in chemical potential the energy-entropy balance in the various phases is significantly shifted to lower temperatures.
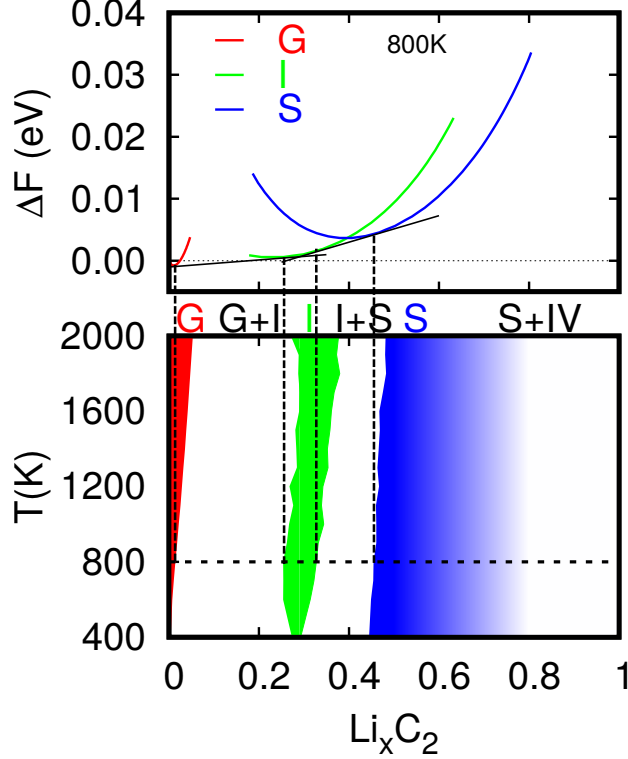
Figure 8: Free energy per site (upper panel) and the phase diagram of Li adsorption on graphene (lower panel). G, I, S and IV represent the gas(red), Li-islands(green), Li-stripes(blue) and islands-of-vacancies respectively. The region between the red and the green is the coexistence between the Li-gas and the Li-island phase while that between the green and the blue region is the region of coexistence between the Li-island and Li-stripes phases. The transition from the Li-stripes phase to island of vacancies as the concentration approaches to 1 is represented by the fading away of the blue region. The vertical dashed lines that extend across the panels are boundaries of the various coexistence regions at 800K.

3D. Li-graphene phase diagram

In order to identify the stable phases for a wide range of concentration and temperature, we construct the Li-graphene phase diagram using the common tangent construction. The common tangent construction at $800\,\mathrm{K}$ and the corresponding phase diagram boundaries are shown in the upper and lower panels of Figure 8, respectively. The maximum concentration at which the Li-gas phase is stable is about $x = 0.05$, equivalent to 1Li:40C at $2000\,\mathrm{K}$, and it decreases progressively with temperature and becomes practically zero at $400\,\mathrm{K}$. Below $400\,\mathrm{K}$, the pure Li-gas phase becomes unstable and only a mixture of the Li-gas and Li-island exists. The region of coexistence between the Li-gas and the Li-island phases extends over a
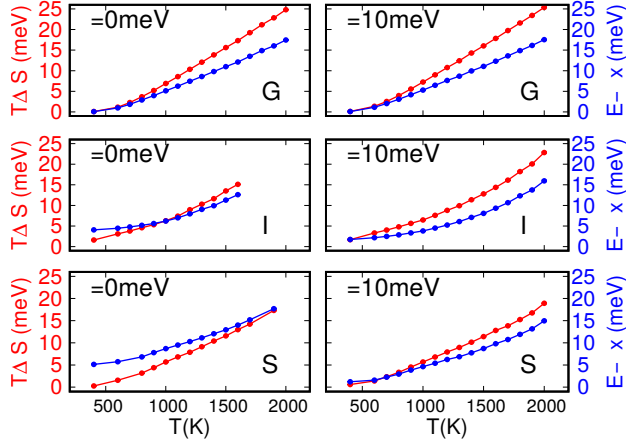
Figure 9: Entropy (red curve) and configurational energy (blue curve) contributions to the free energy as a function of temperature at chemical potential $\mu = 0$ and $\mu = 10\,\mathrm{meV}$. $\mu = 0$ corresponds to the minimum of the Helmholtz free energy. G, I and S represent the Li-gas, the Li-island and the Li-stripe phase respectively.

wide range, up to about $x = 0.3$ ($\approx$1Li:7C). Above $x = 0.3$, the Li-cluster phases are more stable at all temperatures. The stability of the Li-island phase occurs between Li:C$\approx$1:7 and Li:C$\approx$1:5. Between Li:C$\approx$1:5 and Li:C$\approx$1:4, the Li-island phase and the Li-stripe phase coexist in equilibrium. At about $x = 0.5$ (1Li:4C), the Li-stripe phase is the most stable.

The Li-stripe is observed to appear as a result of fusion of large Li-island clusters of adjacent simulation boxes. The stripe configuration hence reduces the surface of Li-clusters and provides an energetically more favorable growth path for increasing concentration, compared to continuous increase in the size of Li-islands. Obviously, in the thermodynamic limit, i.e. in a simulation box of infinite dimension, the fusion of two Li-islands would simply result in another Li-island of larger size and not in an infinitely extended stripe. Thus, in a bigger simulation box, the critical size of Li-island beyond which the Li-stripe will begin to develop is expected to be larger, while other phases such as Li-gas may remain largely unaffected by the size. In order to explore this finite size dependence, we performed simulations similar to the one described so far in a 25x25 graphene supercell, with 1250 carbon atoms and 625 adsorption sites per cell. The results are compared in Figure 10 where the stability domains determined in the larger cell are shown by hatched regions.
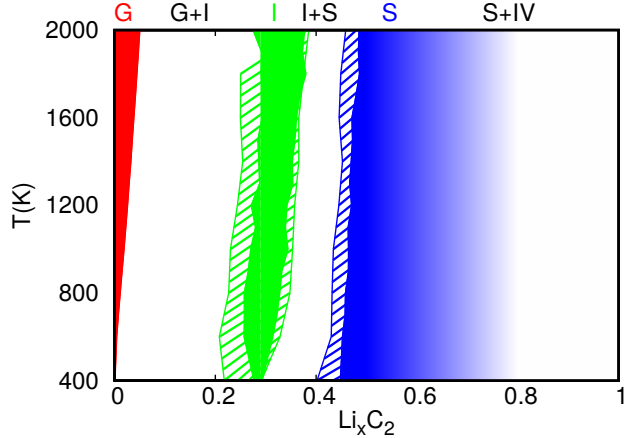
Figure 10: Finite size effect on temperature-concentration phase diagram. The solid shaded regions represent the phase diagram obtained in the 20x20 supercell while the hatched regions correspond to the one of the 25x25 supercell.

The Li-gas phase stability is found to be independent from the size of the simulation box implying that above 400 K and at very low concentration, Li ions will dispersed on graphene surface in the thermodynamic limit. We also observed an increase in the region of stability of Li-island phase with increasing cell size. Considering that in the bigger cell the same concentration is reached with more Li atoms (see Figure S5 in the supplementary material), we see that in the bigger simulation box, bigger islands are stabilized with respect to stripe phase. This confirms the formation of Li-stripes as an artifact of the assumed periodic boundary conditions which would eventually disappear as the cell dimension becomes infinite.

The range of concentration of the phase coexistence regions are also observed to reduce with increasing cell size. This implies that the energy barrier between phases is reduced as the simulation box gets bigger and in the thermodynamic limit the 2D Li adsorption on graphene may occur continuously from Li-gas phase to fully lithiated graphene through the path of gas phase, gas-islands coexistence, Li-island and finally to complete lithiation respectively as the Li concentration increases.

Other phases such as islands-of-vacancies and gas-of-vacancies in an otherwise completely Li-covered graphene were also observed, however these phases are found to be very high in configurational energy. For instance, the energy required to create a single vacancy from

a fully-lithiated graphene according to our model is $1.672\,\mathrm{eV}$ which is about six times the energy required to add a single Li atom to an empty graphene sheet, $0.287\,\mathrm{eV}$. We can estimate the temperature needed to stabilize the gas-of-vacancy phase from the fact that the Li-gas phase is stable at $800\,\mathrm{K}$ and above. Assuming a simple proportionality gives a temperature of about $4800\,\mathrm{K}$.

4. Conclusions

We have presented a study of the interaction of Li with single layer graphene at zero temperature by Density Functional Theory (DFT) and found that Li-graphene interaction is dominated by electrostatics due to charge transfer from Li to graphene. The trend of the adsorption energy per Li was found to be qualitatively different for Li adatoms compared to Li-clusters. This difference was found to be mainly due to drop in the transferred charge in the case of clusters. Li adatoms and small clustered considered were found to be unstable against bulk Li metal at zero temperature. Finite temperature effects were studied by a combination of cluster expansion and Grand Canonical Monte Carlo methods. We found that thermal effects are sufficient to prevent phase separation of the Li-graphene system into its constituents at low concentrations but above the stoichiometry of $\approx \mathrm{LiC_6}$, formation of Li-clusters is energetically favorable with respect to random distribution of Li atoms at all temperatures.

Our study focuses on 2D adsorption. Our systematic approach predicts two stable phases (Li-gas and Li-cluster) and the range of concentration (i.e. the chemical potential) at which the two phases are in equilibrium. This coexistence region, that could not be captured by previous approximate finite temperature treatments, covers about one-third of the entire concentration range at low temperatures. Another phase where Li islands join and form continuous stripes was also observed during Monte Carlo simulations however, by varying the size of the simulation cell, we show that it is due to finite size effects and will eventually

vanish in the thermodynamic limit. Although a simulation artifact in the case of an infinite graphene sheet, such a phase can be speculated to occur at the edges of a graphene flake and seed the lithiation.

While 3D configurations could in principle be considered and were previously theoretically shown to be more stable with respect to random distribution of Li atoms both by zero-[19] and approximate finite-temperature calculations,[20,21] our 2D study may help interpret some interesting experimental observations such as the evidence of enhanced Li capacity in spatially constrained graphene materials where Li uptake positively correlates with the average interlayer distance. For example Ref. 8 reports that increasing the interlayer distance from 3.6 Å to 4.0 Å increases the capacity from 320 mAh/g, less than graphite, to 784 mAh/g, more than twice of graphite. In such densely packed, spatially constrained graphene materials, Li coverage model is more compatible with 2D rather than 3D clustering, and the increase in Li uptake with increasing interlayer spacing is compatible with a gradual transition from 2D to 3D cluster formation. Therefore, combined with these experimental observations in the literature, our results suggest that high Li uptake in dense graphene materials may be the result of significant 2D Li clustering. The computationally demanding study of vibrational effects, such as population of flexural phonons of graphene that may further stabilize Li adsorption, is left for future work.

Supporting Information Available

Effect of periodic boundary conditions along the perpendicular direction to graphene plane, details of the fitting procedure of the cluster expansion model, results of several variants of the model and Li-graphene phase diagram as a function of number of Li.

Acknowledgement

References

(1) Choi, J. W.; Aurbach, D. Promise and Reality of Post-Lithium-Ion Batteries With High Energy Densities. *Nature Reviews Materials* **2016**, *1*, 16013.

(2) Yazami, R.; Touzain, P. A Reversible Graphite-Lithium Negative Electrode for Electrochemical Generators. *Journal of Power Sources* **1983**, *9*, 365–371.

(3) Winter, M.; Besenhard, J. O.; Spahr, M. E.; Novak, P. Insertion Electrode Materials for Rechargeable Lithium Batteries. *Advanced Materials* **1999**, *10*, 725–763.

(4) Guerard, D.; Herold, A. Intercalation of Lithium Into Graphite and Other Carbons. *Carbon* **1975**, *13*, 337–345.

(5) Novoselov, K. S.; Geim, A. K.; Morozov, S. V.; Jiang, D.; Zhang, Y.; Dubonos, S. V.; Grigorieva, I. V.; Firsov, A. A. Electric Field Effect in Atomically Thin Carbon Films. *Science* **2004**, *306*, 666–669.

(6) Dahn, J. R.; Zheng, T.; Liu, Y.; Xue, J. S. Mechanisms for Lithium Insertion in Carbonaceous Materials. *Science* **1995**, *270*, 590–593.

(7) Pollak, E.; Geng, B.; Jeon, K.-J.; Lucas, I. T.; Richardson, T. J.; Wang, F.; Kostecki, R. The Interaction of Li+ with Single-Layer and Few-Layer Graphene. *Nano Lett.* **2010**, *10*, 3386–3388.

(8) Yoo, E.; Kim, J.; Hosono, E.; Zhou, H.-S.; Kudo, T.; Honma, I. Large Reversible Li

Storage of Graphene Nanosheet Families for Use in Rechargeable Lithium Ion Batteries. *Nano Letters* **2008**, *8*, 2277–2282.

(9) Wang, G.; Shen, X.; Yao, J.; Park, J. Graphene Nanosheets for Enhanced Lithium Storage in Lithium Ion Batteries. *Carbon* **2009**, *47*, 2049 – 2053.

(10) Hassoun, J.; Bonaccorso, F.; Agostini, M.; Angelucci, M.; Betti, M. G.; Cingolani, R.; Gemmi, M.; Mariani, C.; Panero, S.; Pellegrini, V. et al. An Advanced Lithium-Ion Battery Based on a Graphene Anode and a Lithium Iron Phosphate Cathode. *Nano Lett.* **2014**, *14*, 4901–4906.

(11) Wang, B.; Ryu, J.; Choi, S.; Song, G.; Hong, D.; Hwang, C.; Chen, X.; Wang, B.; Li, W.; Song, H.-K. et al. Folding Graphene Film Yields High Areal Energy Storage in Lithium-Ion Batteries. *ACS Nano* **2018**, *12*, 1739–1746, PMID: 29350526.

(12) Sun, H.; Mei, L.; Liang, J.; Zhao, Z.; Lee, C.; Fei, H.; Ding, M.; Lau, J.; Li, M.; Wang, C. et al. Three-Dimensional Holey-Graphene/Niobia Composite Architectures for Ultrahigh-Rate Energy Storage. *Science* **2017**, *356*, 599–604.

(13) Lee, E.; Persson, K. A. Li Absorption and Intercalation in Single Layer Graphene and Few Layer Graphene by First Principles. *Nano Lett.* **2012**, *12*, 4624–4628.

(14) Zhou, L.-J.; Hou, Z. F.; Wu, L.-M. First-Principles Study of Lithium Adsorption and Diffusion on Graphene With Point Defects. *The Journal of Physical Chemistry C* **2012**, *116*, 21780–21787.

(15) Okamoto, Y. Density Functional Theory Calculations of Lithium Adsorption and Insertion to Defect-Free and Defective Graphene. *The Journal of Physical Chemistry C* **2016**, *120*, 14009–14014.

(16) Uthaisar, C.; Barone, V.; Peralta, J. E. Lithium Adsorption on Zigzag Graphene Nanoribbons. *Journal of Applied Physics* **2009**, *106*, 113715.

(17) Leggesse, E. G.; Chen, C.-L.; Jiang, J.-C. Lithium Diffusion in Graphene and Graphite: Effect of Edge Morphology. *Carbon* **2016**, *103*, 209–216.

(18) Fan, X.; Zheng, W. T.; Kuo, J.-L. Adsorption and Diffusion of Li on Pristine and Defective Graphene. *ACS Applied Materials & Interfaces* **2012**, *4*, 2432–2438.

(19) Fan, X.; Zheng, W. T.; Kuo, J.-L.; Singh, D. J. Adsorption of Single Li and the Formation of Small Li Clusters on Graphene for the Anode of Lithium-Ion Batteries. *ACS Applied Materials & Interfaces* **2013**, *5*, 7793–7797.

(20) Liu, M.; Kutana, A.; Liu, Y.; Yakobson, B. I. First-Principles Studies of Li Nucleation on Graphene. *The Journal of Physical Chemistry Letters* **2014**, *5*, 1225–1229.

(21) Yang, G.; Fan, X.; Liang, Z.; Xu, Q.; Zheng, W. Density Functional Theory Study of Li Binding to Graphene. *RSC Adv.* **2016**, *6*, 26540–26545.

(22) Hohenberg, P.; Kohn, W. Inhomogeneous Electron Gas. *Phys. Rev.* **1964**, *136*, B864–B871.

(23) Kohn, W.; Sham, L. J. Self-Consistent Equations Including Exchange and Correlation Effects. *Phys. Rev.* **1965**, *140*, A1133–A1138.

(24) Blöchl, P. E. Projector Augmented-Wave Method. *Phys. Rev. B* **1994**, *50*, 17953–17979.

(25) Giannozzi, P.; Baroni, S.; Bonini, N.; Calandra, M.; Car, R.; Cavazzoni, C.; Ceresoli, D.; Chiarotti, G. L.; Cococcioni, M.; Dabo, I. et al. QUANTUM ESPRESSO: A Modular and Open-Source Software Project for Quantum Simulations of Materials. *Journal of Physics: Condensed Matter* **2009**, *21*, 395502.

(26) Giannozzi, P.; Andreussi, O.; Brumme, T.; Bunau, O.; Nardelli, M. B.; Calandra, M.; Car, R.; Cavazzoni, C.; Ceresoli, D.; Cococcioni, M. et al. Advanced Capabilities for Materials Modelling with Quantum ESPRESSO. *Journal of Physics: Condensed Matter* **2017**, *29*, 465901.

(27) Dal Corso, A. Pseudopotentials Periodic Table: From H to Pu. *Computational Materials Science* **2014**, *95*, 337–350.

(28) Vydrov, O. A.; Voorhis, T. V. Nonlocal Van Der Waals Density Functional: The Simpler the Better. *The Journal of Chemical Physics* **2010**, *133*, 244103.

(29) Sabatini, R.; Gorni, T.; de Gironcoli, S. Nonlocal Van Der Waals Density Functional Made Simple and Efficient. *Phys. Rev. B* **2013**, *87*, 041108.

(30) Perdew, J. P.; Burke, K.; Ernzerhof, M. Generalized Gradient Approximation Made Simple. *Phys. Rev. Lett.* **1996**, *77*, 3865–3868.

(31) Monkhorst, H. J.; Pack, J. D. Special Points for Brillouin-Zone Integrations. *Phys. Rev. B* **1976**, *13*, 5188–5192.

(32) Methfessel, M.; Paxton, A. T. High-Precision Sampling for Brillouin-Zone Integration in Metals. *Phys. Rev. B* **1989**, *40*, 3616–3621.

(33) Chan, K. T.; Neaton, J. B.; Cohen, M. L. First-Principles Study of Metal Adatom Adsorption on Graphene. *Phys. Rev. B* **2008**, *77*, 235430.

(34) Praveen, C. S.; Piccinin, S.; Fabris, S. Adsorption of Alkali Adatoms on Graphene Supported by the Au/Ni(111) Surface. *Phys. Rev. B* **2015**, *92*, 075403.

(35) Baskin, Y.; Meyer, L. Lattice Constants of Graphite at Low Temperatures. *Phys. Rev.* **1955**, *100*, 544–544.

(36) Yata, S.; Kinoshita, H.; Komori, M.; Ando, N.; Kashiwamura, T.; Harada, T.; Tanaka, K.; Yamabe, T. Structure and Properties of Deeply Li-Doped Polyacenic Semiconductor Materials Beyond C6Li Stage. *Synthetic Metals* **1994**, *62*, 153–158.

(37) Laks, D. B.; Ferreira, L. G.; Froyen, S.; Zunger, A. Efficient Cluster Expansion for Substitutional Systems. *Phys. Rev. B* **1992**, *46*, 12587–12605.

(38) Metropolis, N.; Rosenbluth, A. W.; Rosenbluth, M. N.; Teller, A. H.; Teller, E. Equation of State Calculations by Fast Computing Machines. *The Journal of Chemical Physics* **1953**, *21*, 1087–1092.

(39) Hastings, W. K. Monte Carlo Sampling Methods Using Markov Chains and Their Applications. *Biometrika* **1970**, *57*, 97–109.

(40) Garay-Tapia, A. M.; Romero, A. H.; Barone, V. Lithium Adsorption on Graphene: From Isolated Adatoms to Metallic Sheets. *Journal of Chemical Theory and Computation* **2012**, *8*, 1064–1071.

(41) Uthaisar, C.; Barone, V. Edge Effects on the Characteristics of Li Diffusion in Graphene. *Nano Letters* **2010**, *10*, 2838–2842.

(42) Yildirim, H.; Kinaci, A.; Zhao, Z.-J.; Chan, M. K. Y.; Greeley, J. P. First-Principles Analysis of Defect-Mediated Li Adsorption on Graphene. *ACS Applied Materials & Interfaces* **2014**, *6*, 21141–21150.

(43) Persson, K.; Hinuma, Y.; Meng, Y. S.; Van der Ven, A.; Ceder, G. Thermodynamic and Kinetic Properties of the Li-Graphite System From First-Principles Calculations. *Phys. Rev. B* **2010**, *82*, 125416.

Graphical TOC Entry
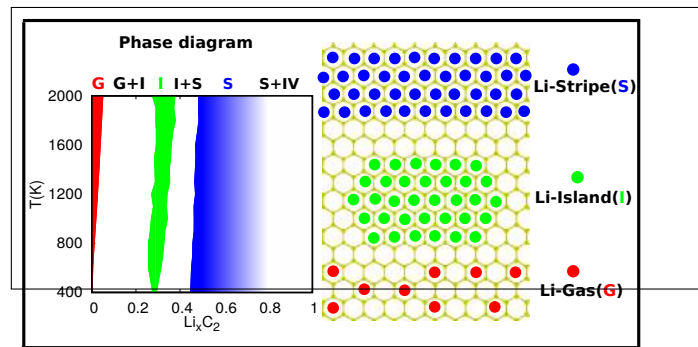
Lithium Adsorption on Graphene at Finite Temperature

Yusuf Shaidu,[†,‡] Emine Kucukbenli,[‡] and Stefano de Gironcoli[*,‡]

†*The Abdus Salam International Centre for Theoretical Physics, Trieste, Italy*

‡*International School for Advanced Studies, Trieste, Italy*

E-mail: degironc@sissa.it

Effect of periodic boundary conditions along the aperiodic direction

Here we give a brief analysis of the effect of periodic boundary conditions (PBC) on energetics reported in the main article. In our calculations, the vacuum size between adjacent graphene sheets is set to 20 Å. To demonstrate the impact of this parameter on the adsorption energy, we perform Li adatom adsorption calculations on a 3x3 graphene supercell while varying the vacuum size, i.e. graphene layer separation (LS) between 10 and 30 Å. The single Li adatom on graphene case has the highest amount of charge transfer, therefore, it is expected to have the most pronounced long-range electrostatic behaviour between graphene sheets. Hence the error reported here can be seen as an upper bound to the impact of PBC.
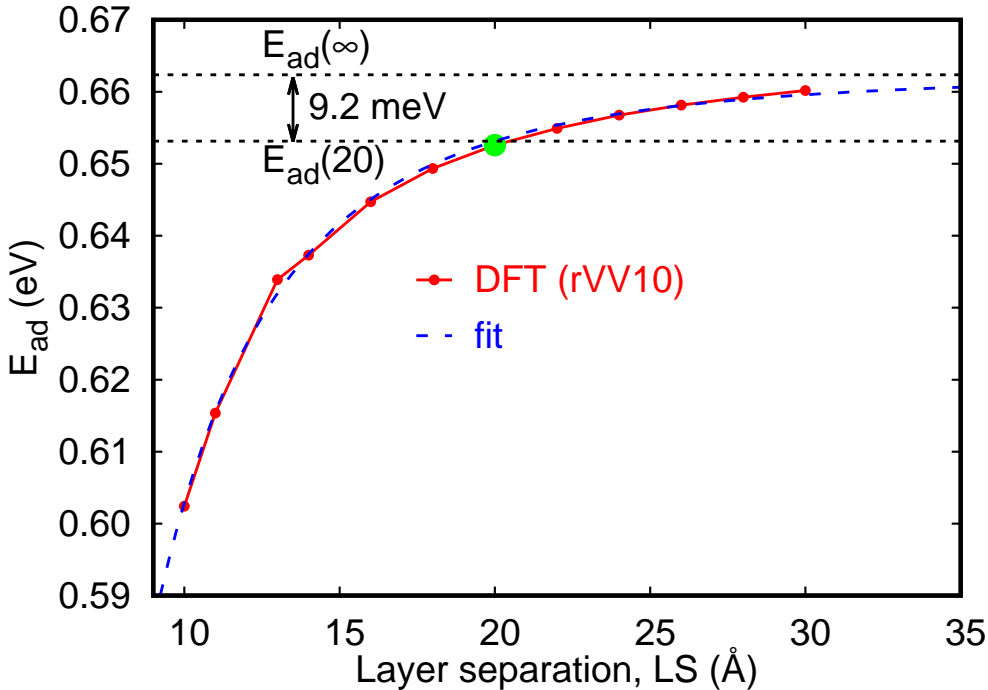

Figure S1: Adsorption energy(E_{ad}) of Li adatom on the hollow site of 3x3 graphene supercell as a function layer separation (LS). The infinite layer separation limit, $E_{ad}(\infty)$ was obtained via fitting using Eq.1. The parameters of the fit are $E_{ad}(\infty) = 0.662362$, b=-3.04981;c=3.05586. R is the nearest neighbor distance for Li in-plane, R=3×2.47 Å in the case of 3x3 supercell. The root-mean-square (rms) error of the fit is 0.77 meV.

Fig. S1 shows the adsorption energy, E_{ad} referenced to bulk Li as a function of layer

separation (LS). In order to estimate the adsorption energy at infinite separation, we fit the DFT data (red curve of Fig. S1) to a simple function of LS and the in-plane distance between Li adatoms on surface , R:

$$E(LS) = E_{ad}(\infty) + \frac{b}{LS} + \frac{c}{\sqrt{(R^2 + LS^2)}} \tag{1}$$

This functional form mimics the Coulomb interaction of Li adatom and its periodic images on adjacent graphene layers, as well as the interaction with the periodic images of its nearest neighbors. Therefore at infinite layer separation, we can approximate the energy as $E_{ad}(\infty)$. The difference in adsorption energy between LS=∞ and LS=20 Å is estimated to be 9.2 meV. This value is smaller than the energy difference between Li-adatom and Li-cluster phases at 0K (which ranges between 44 and 176 meV on a 3x3 supercell and between 149 and 312 meV on a 6x6 supercell). Therefore the results calculated at LS=20 Å can be considered as a good approximation to the infinite separation limit for the analysis of phase stability at 0 K.

We can confirm this by observing the electronic density profile as well: The planar average of the charge density difference in Fig. S2 shows that the charge density profile does not change significantly at layer separations above 16 Å.

The impact of PBC on the model that is used in finite temperature study can be analyzed as follows: The cluster expansion interaction potential is obtained via a fit to DFT energies. The standard deviation of this fit is 18.0 meV, while the upper-bound of the correction due to PBC is estimated to be $\approx$9 meV using the fit demonstrated above. Thus, the results calculated at LS=20 Å can be considered as a good approximation to the infinite separation limit for the analysis of phase stability also at finite temperatures.
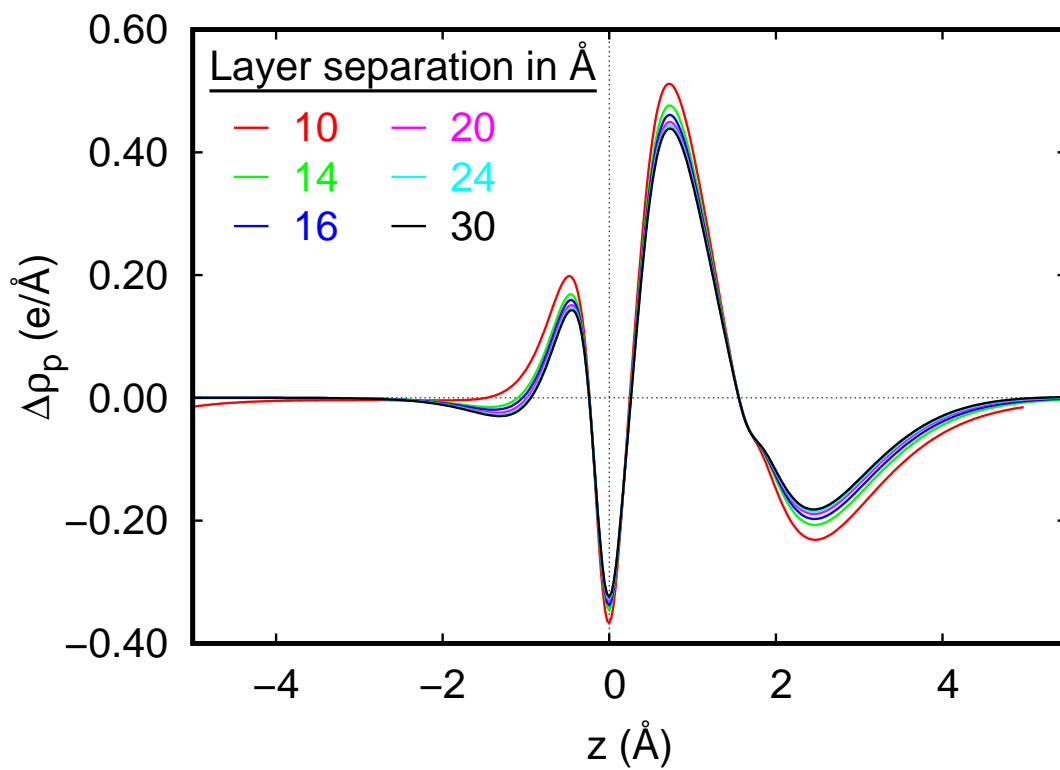
Figure S2: The planar average of the charge density difference between pristine graphene and Li-adsorpbed graphene, $\Delta\rho_p(z) = \int \Delta\rho(x, y, z)dxdy$, plotted at different graphene layer separations as a function of the perpendicular distance from the graphene plane (situated at $z = 0\,\text{Å}$)

Fitting procedure

The performance of the Cluster Expansion model was optimized by minimizing the standard deviation, σ, of the adsorption energies predicted by the model from the adsorption energies obtained by density functional theory (DFT). In order to avoid overfitting and favor locality, a penalty term to the cost function was added. The penalty matrix was defined so that the two body interactions are penalized proportionally to the distance of the interacting pairs; for instance, the element for second nearest neighbor interaction is multiplied by $(\sqrt{3.0})^\lambda$. This imposed locality constraints to the 2-body terms similar to the one developed in Ref. 1. The total cost function per Li is defined as

$$\sigma_{Li}^2 = \frac{1}{N_{config}} \sum_{i=1}^{N_{config}} \left[\frac{E_{DFT}^i - E_{CE}^i}{N_{Li}} \right]^2 + t \sum_{i=1}^{N_J} J_i M_i J_i, \tag{2}$$

where the accuracy of the model is defined as

$$\sigma_{Li}^2 = \frac{1}{N_{config}} \sum_{i=1}^{N_{config}} \left[\frac{E_{DFT}^i - E_{CE}^i}{N_{Li}} \right]^2 = \frac{1}{N_{config}} \sum_{i=1}^{N_{config}} \sigma_i^2, \tag{3}$$

and σ_i^2 is the square deviation per Li of the model adsorption energy of configuration i from DFT one.

Similarly, the mean square deviation per carbon is given by

$$\sigma_C^2 = \frac{1}{N_{config}} \sum_{i=1}^{N_{config}} \left(\frac{N_{Li}}{N_C} \right)^2 \sigma_i^2. \tag{4}$$

In matrix form the cluster expansion for a given configuration C is given by

$$E_{CE}(C) = \sum_f J_f \Pi_f(C) \tag{5}$$

and the cost function per Li atom is given by

$$\sigma_{Li}^2 = \frac{1}{N_{config}} \sum_C (E_{DFT} - \Pi J)^T (E_{DFT} - \Pi J) + t J^T M J. \tag{6}$$

Here, M is a diagonal matrix with elements that depend on the range of J for 2-body interactions and 1.0 otherwise. We used $t = 0.0005$ and $\lambda = 1.0$. Thus, the extra cost associated with the locality constraint is minimal and only play a significant role when less configurations than parameters are fitted.

Fitted configurations

The fitted configurations are Li-adatom in 2x2 to 8x8 supercell, Li-dimer in 3x3 to 7x7 supercells, Li-trimer in 3x3 to 7x7 supercells and Li-tetramer in 3x3 to 6x6 supercells , the 5- and 6-Li atom clusters in the 4x4 supercell of graphene and those shown in Fig. S3 which are mixture of clusters and adatoms.
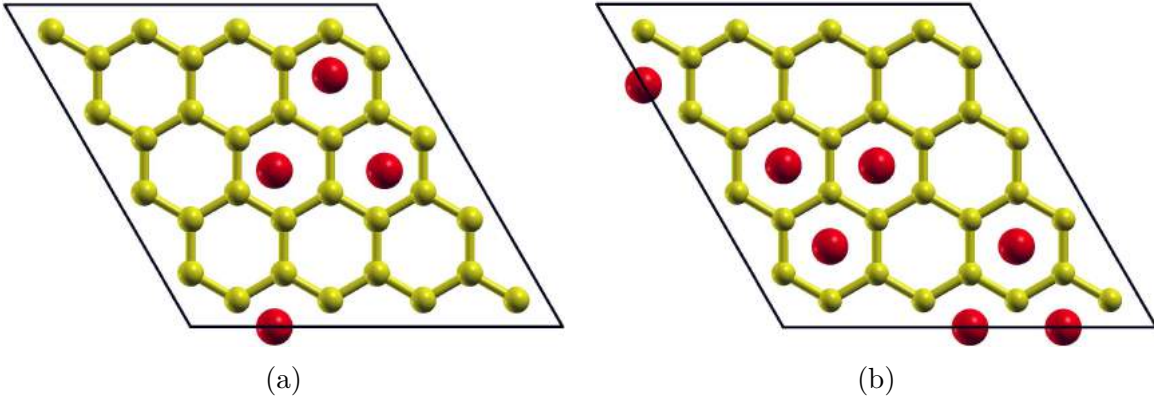

(a)   (b)

Figure S3: A pair of generic Li atom configurations in a 4x4 graphene supercell with (a) 4 Li atoms per unit cell and (b) 7 Li atoms per unit cell.
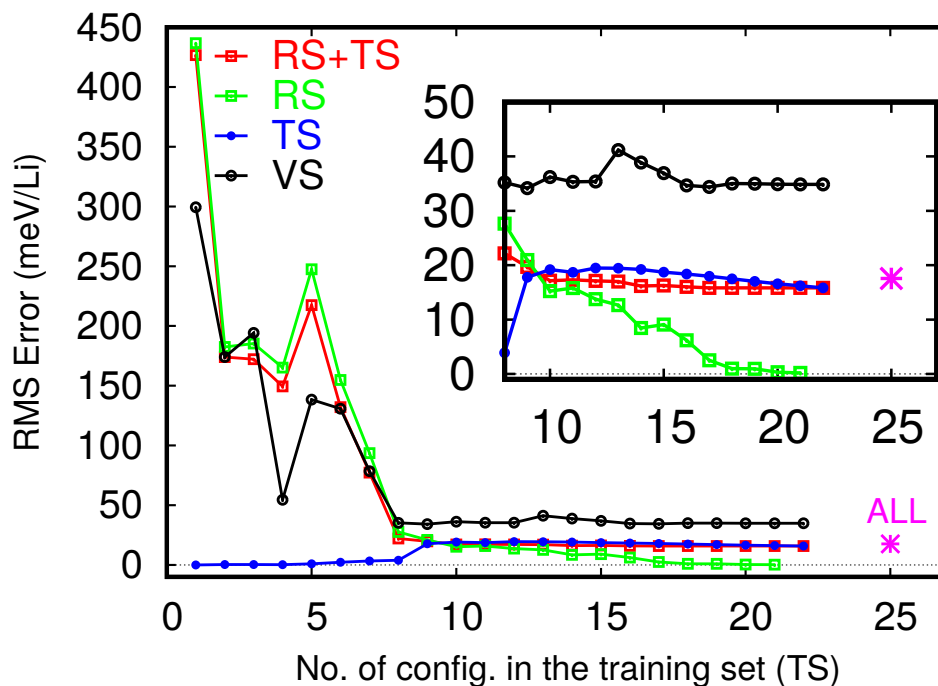
Monitoring the fitting procedure

Figure S4: Evolution of the root-mean-square (RMS) error as the number of configurations used in fitting, i.e. in the training set (TS), increases. In this analysis, we use a total of 25 different configurations of Li on graphene. Three configurations are set aside as validation set (VS) and are never included during the training of the model. Therefore, at zeroth step of the training, we have zero configurations in the training set (TS) and 22 configurations in the remaining set (RS). At each step of the training the configuration with the largest prediction error is added to TS, reducing the number of configurations in the RS by one. We continue these training steps until all 22 configurations in RS have been added to TS. Finally, for analysis purposes we also perform a training including all 25 configurations (magenta asterisk labeled as ALL). The inset shows the zoom of the plot at later steps of training where RMS error converges for TS.

Performance of the model

In Fig. S5 the deviation of the DFT energy from the energy predicted by the full model described in the manuscript is shown. The root-mean-square deviation is $18.0\,\text{meV/Li}$ ($1.6\,\text{meV/C}$) with a cross validation error of $30.2\,\text{meV/Li}$ ($3.2\,\text{meV/C}$) as already reported in the main text.
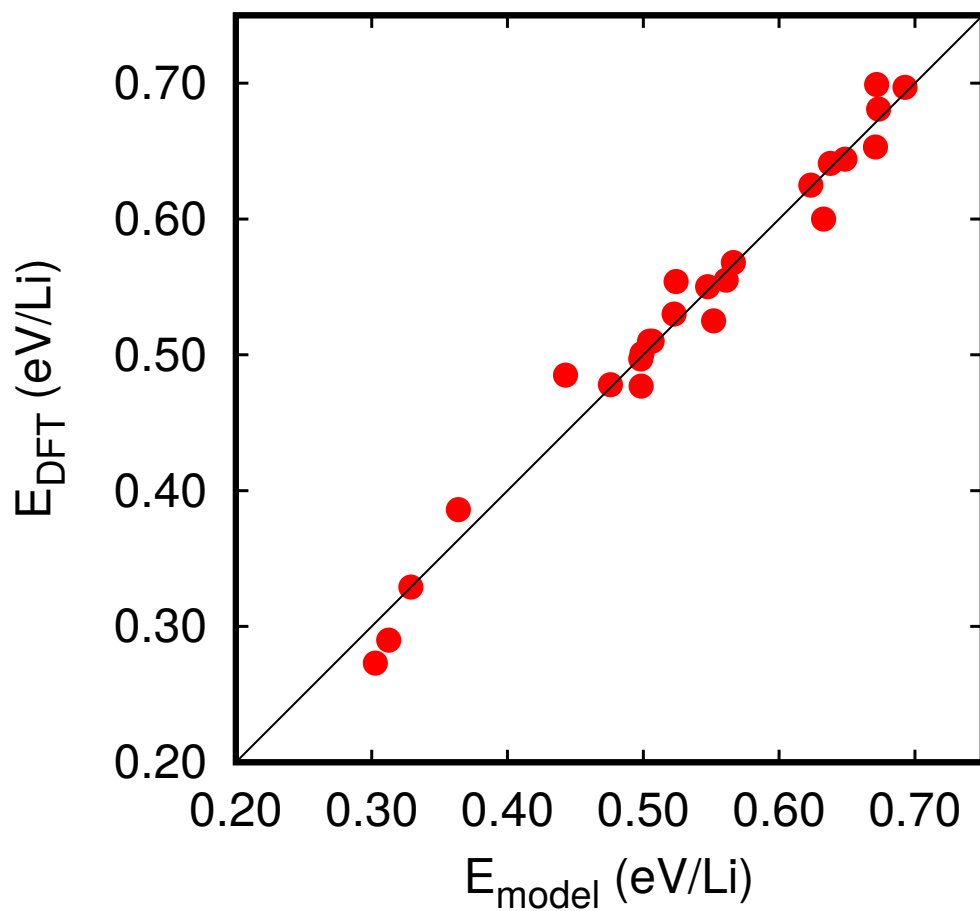
Figure S5: Comparison of the model energies with DFT ones using rVV10 functional. The black line represents perfect agreement while the red points are the actual model predictions.

Table S1: Best fit values for the effective cluster interactions of the model when 3- and 4-body interaction terms are neglected. All parameters, except γ, in eV.

	J_1	J_{2a}	J_{2b}	J_{2c}	J_3	J_4	J_{dd}	γ
ECI	0.429	0.074	-0.177	0.051	0.000	0.000	1.198	0.559

When 3- and 4-body terms are neglected, the obtained results are similar to the one reported in Ref. 2: the most influential cluster figure is the point cluster as shown in table S1. The resulting root-mean-square deviation is $98.3 \, \mathrm{meV/Li}$ ($7.5 \, \mathrm{meV/C}$) with a cross validation error of $158.2 \, \mathrm{meV/Li}$ ($21.2 \, \mathrm{meV/C}$). The reduced quality of the model is shown in Fig. S6.
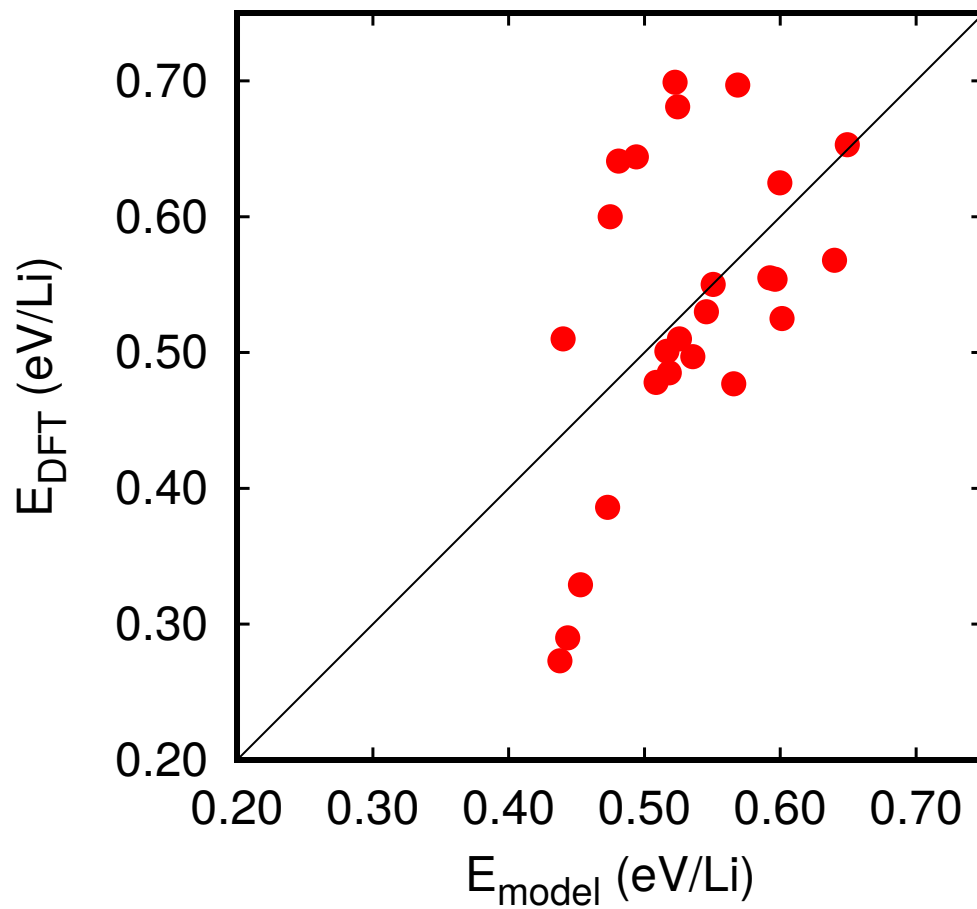
Figure S6: Comparison of the model energies with DFT ones using rVV10 functional when 3- and 4-body interaction terms are neglected. The black line represents perfect agreement while the red points are the actual model predictions.

Even less accurate results are obtained when in addition, the J_{dd} term is set to zero. Results are reported in table S2. The root-mean-square deviation is $108.3\,\text{meV/Li}$ $(7.3\,\text{meV/C})$ with a cross validation error of $133.9\,\text{meV/Li}$ ($15.3\,\text{meV/C}$). The DFT vs model comparison is shown in Fig. S7. This is a strong indication that the long-range dipole-dipole term and the 3- and 4- body interactions are very important for a proper description of Li adsorption on graphene.

Table S2: Best fit values for the effective cluster interactions of the model when 3- and 4-body and long-range interaction terms are neglected. All parameters, except γ, in eV

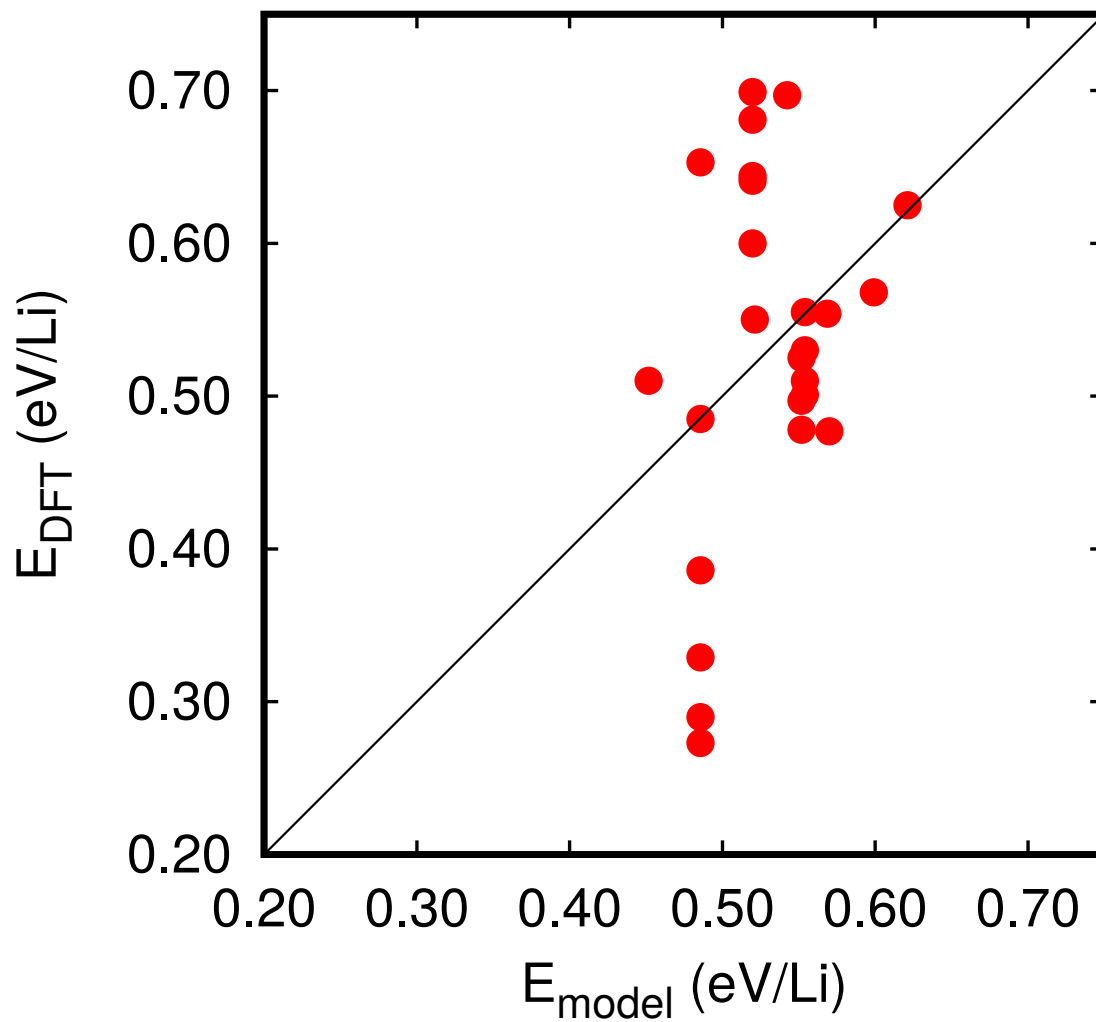|	J_1	J_{2a}	J_{2b}	J_{2c}	J_3	J_4	J_{dd}	γ
ECI	0.486	0.068	-0.077	0.045	0.000	0.000	0.0000	0.000

Figure S7: Comparison of the model energies with DFT ones using rVV10 functional when 3- and 4-body and long-range interaction terms are neglected. The black line represents perfect agreement while the red points are the actual model predictions.

When only the dipole-dipole long-range terms are neglected the resulting parameters are the ones reported in table S3 (DFT *vs* model deviations shown in Fig. S8). This model describes relatively well the Li-dense configurations, but dilute configurations with Li adatoms in 3x3 to 8x8 are poorly described indicating the importance of the long-range dipole-dipole interaction term.

The root-mean-square deviation is $70.9\,\mathrm{meV/Li}$ ($5.2\,\mathrm{meV/C}$) with a cross validation error of $91.9\,\mathrm{meV/Li}$ ($8.6\,\mathrm{meV/C}$)

Table S3: Best fit values for the effective cluster interactions of the model when only the dipole-dipole long-range terms are neglected. All parameters, except γ, in eV

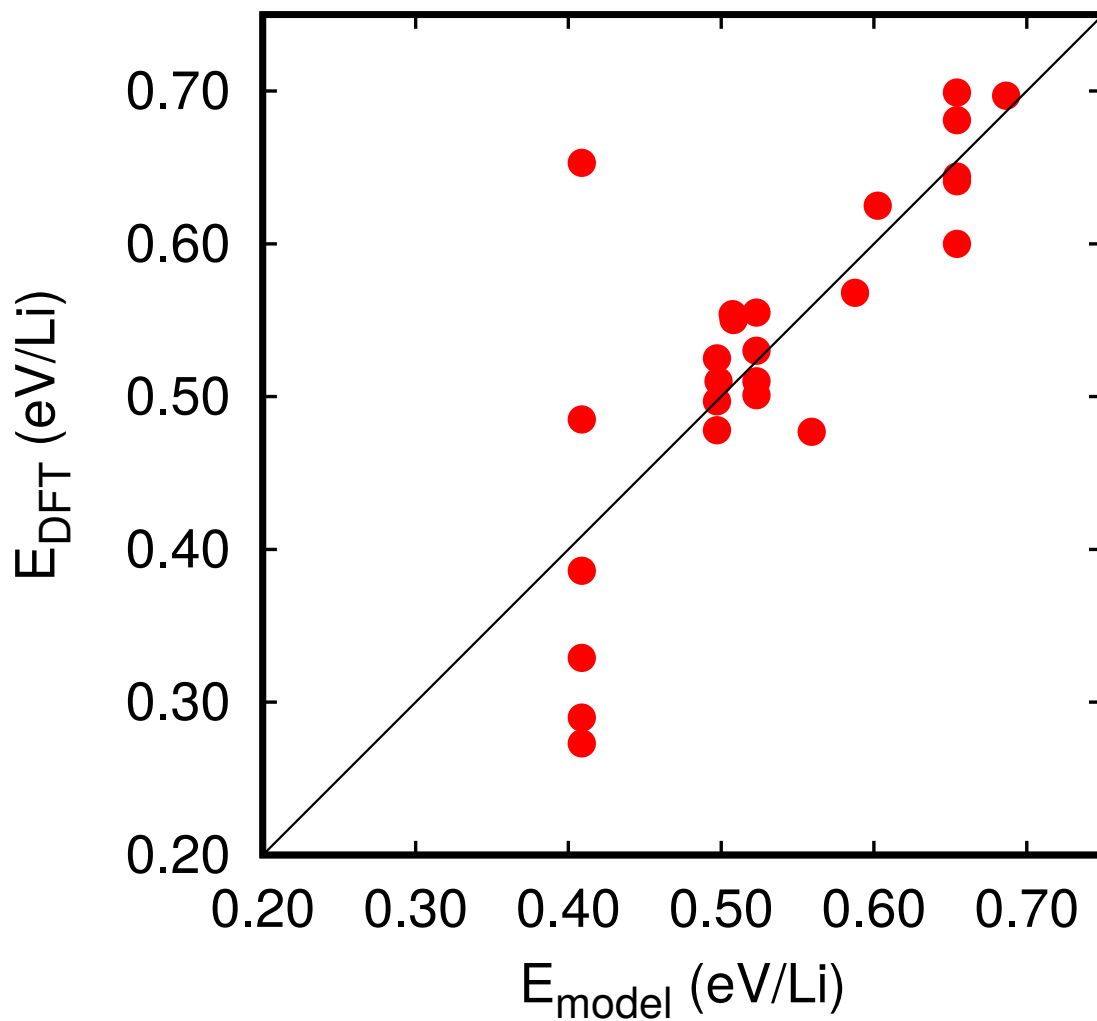|	J_1	J_{2a}	J_{2b}	J_{2c}	J_3	J_4	J_{dd}	γ
ECI	0.408	0.491	-0.037	0.065	-1.130	0.196	0.0000	0.000

Figure S8: Comparison of the model energies with DFT ones using rVV10 functional when only the long-range interaction terms are neglected. The black line represents perfect agreement while the red points are the actual model predictions.

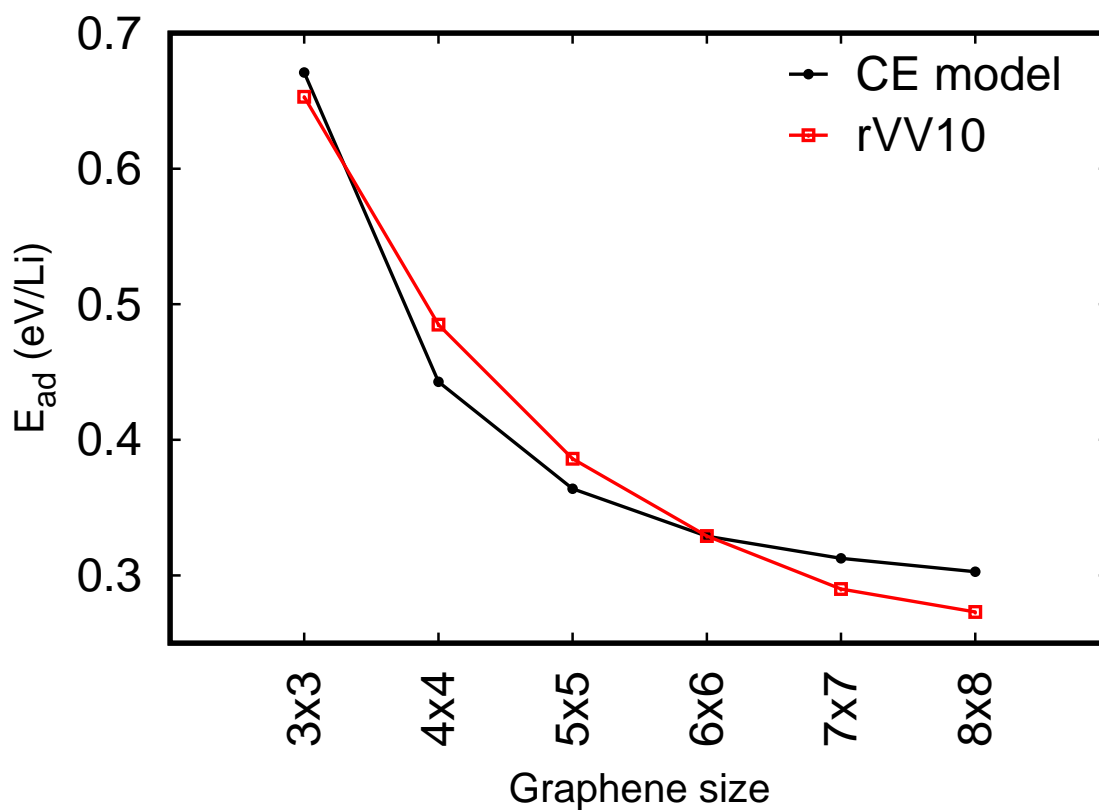# Cluster Expansion : The behaviour of the dipole-dipole interaction term

Figure S9: The behaviour of the dipole-dipole part of the cluster expansion model obtained via single Li adatom on various supercell sizes. Note that in all the supercell sizes used, Li ions in adjacent cells are far enough that the only contributions to the model energy are the onsite term, which constitutes a constant shift, and the long-range interaction term. The model can be seen to capture the long-range behaviour observed in the DFT calculations (red squares)
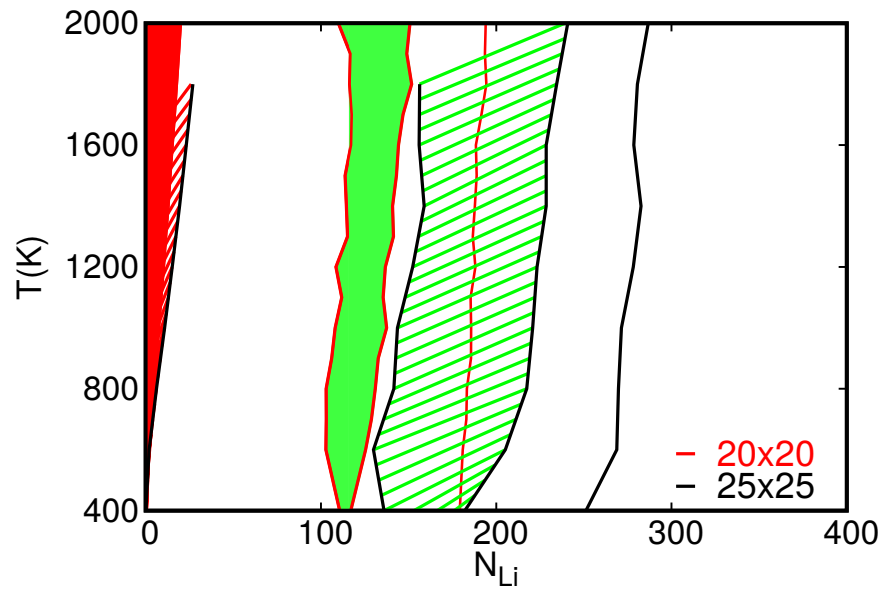
Finite size analysis

Figure S10: Finite size effects: Temperature versus number of Li N_{Li} phase diagram. The red lines represent the phase boundaries determined with a 20x20 supercell and the black lines represent those determined with the 25x25 supercell. The red and green shaded region are the Li-gas and Li-island phases in a 20x20 cell while the red and green hatch regions are corresponds to those obtained with 25x25 supercell. The plot shows the increased dimension of the Li-islands in equilibrium with the Li-stripe phase as a function of the similation box size.

References

(1) Laks, D. B.; Ferreira, L. G.; Froyen, S.; Zunger, A. Efficient Cluster Expansion for Substitutional Systems. *Phys. Rev. B* **1992**, *46*, 12587–12605.

(2) Lee, E.; Persson, K. A. Li Absorption and Intercalation in Single Layer Graphene and Few Layer Graphene by First Principles. *Nano Lett.* **2012**, *12*, 4624–4628.